Draft version July 1, 2011
Preprint typeset using LaTeX style emulateapj v. 11/10/09

THE r-PROCESS IN THE NEUTRINO-DRIVEN WIND FROM A BLACK-HOLE TORUS

Shinya Wanajo[1, 2] and Hans-Thomas Janka[2]

Draft version July 1, 2011

ABSTRACT

We examine r-process nucleosynthesis in the neutrino-driven wind from the thick accretion disk (or "torus") around a black hole. Such systems are expected as remnants of binary neutron star or neutron star – black hole mergers. We consider a simplified, analytic, time-dependent evolution model of a $3M_\odot$ central black hole surrounded by a neutrino emitting accretion torus with 90 km radius, which serves as basis for computing spherically symmetric neutrino-driven wind solutions. We find that ejecta with modest entropies (~ 30 per nucleon in units of the Boltzmann constant) and moderate expansion timescales (~ 100 ms) dominate in the mass outflow. The mass-integrated nucleosynthetic abundances are in good agreement with the solar system r-process abundance distribution if a minimal value of the electron fraction at the charged-particle freezeout, $Y_{\rm e,min} \sim 0.2$, is achieved. In the case of $Y_{\rm e,min} \sim 0.3$, the production of r-elements beyond $A \sim 130$ does not reach to the third peak but could be still important for an explanation of the abundance signatures in r-process deficient stars in the early Galaxy. The total mass of the ejected r-process nuclei is estimated to be $\sim 1 \times 10^{-3} M_\odot$. If our model was representative, this demands a Galactic event rate of $\sim 2 \times 10^{-4}$ yr^{-1} for black-hole-torus winds from merger remnants to be the dominant source of the r-process elements. Our result thus suggests that black-hole-torus winds from compact binary mergers have the potential to be a major but probably not the dominant production site of r-process elements.

Subject headings: nuclear reactions, nucleosynthesis, abundances — binaries: close — stars: abundances — stars: neutron

1. INTRODUCTION

In the past decades, core-collapse supernovae (CCSNe) have been considered to be the most promising astrophysical site for providing physical conditions suitable for the r(rapid neutron capture)-process (see, e.g., Thielemann et al. 2011, for a recent review). The scenarios include the neutrino-driven wind of CCSNe (Woosley et al. 1994; Takahashi et al. 1994; Qian & Woosley 1996; Otsuki et al. 2000; Wanajo et al. 2001; Thompson et al. 2001; Farouqi et al. 2010), prompt explosions of CCSNe (Sumiyoshi et al. 2001) or of electron-capture supernovae (ECSNe; a subset of CCSNe arising from collapsing oxygen-neon-magnesium cores, Hillebrandt et al. 1984; Wanajo et al. 2003), and the shocked surface layers of the stellar core in collapsing ECSNe (Ning et al. 2007).

However, recent hydrodynamical simulations of CCSNe (e.g., Buras et al. 2006; Marek & Janka 2009) and of ECSNe (Kitaura et al. 2006; Janka et al. 2008) do not support the prompt explosion or the shocked surface layer scenarios. The nucleosynthesis calculations with one-dimensional hydrodynamical results of ECSNe do not confirm the production of elements beyond $A \sim 90$, either (Hoffman et al. 2008; Wanajo et al. 2009). Furthermore, recent long-term simulations of CCSNe and ECSNe show that the neutrino-driven outflows are proton-rich all the way (Fischer et al. 2010; Hüdepohl et al. 2010), which poses a severe difficulty to the scenario that has been favored for a long time, neutrino-driven winds from proto-neutron stars (PNSs) in CCSNe and ECSNe. Recently, Wanajo et al. (2011a) suggested on the basis of two-dimensional models of ECSNe that a weak r-process could lead to the production of trans-iron elements in the early neutron-rich convective blobs of such SNe, but no heavier than $A \sim 120$.

In contrast, another popular scenario of the astrophysical r-process, the mergers of double neutron stars (NS-NS, e.g., Rosswog et al. 1999; Ruffert & Janka 1999; Shibata & Uryū 2000; Shibata & Taniguchi 2006; Oechslin et al. 2007) or of black hole – neutron star binaries (BH-NS, e.g., Janka et al. 1999; Shibata & Uryū 2006; Ruffert & Janka 2010), has not been satisfactorily explored. The decompression of dynamically ejected neutron-rich crust matter from NS-NS (or BH-NS) mergers was suggested to be an alternative or additional r-process site (Lattimer & Schramm 1974, 1976; Lattimer et al. 1977; Meyer 1989; Freiburghaus et al. 1999; Goriely et al. 2005, 2011). Hyper-massive NSs (HMNSs) resulting immediately after NS-NS merging (e.g., Sekiguchi et al. 2011; Rezzolla et al. 2011; Bauswein & Janka 2011), giving rise to magnetically driven and neutrino-driven outflows for $\sim$ 10-100 ms, are also suggested to eject r-processed material (Dessart et al. 2009). Furthermore, both NS-NS (after a possibly only short HMNS phase) and BH-NS (without a HMNS phase) mergers are expected to form a neutrino radiating accretion torus around the relic black hole, giving rise to neutrino-driven winds (hereafter, BH-torus winds) and potential short-duration gamma-ray-burst (GRB) jets. BH-torus winds are also expected to provide suitable physical conditions for the r-process (Ruffert & Janka 1999; Surman et al. 2008; Metzger et al. 2008).

[1] Technische Universität München, Excellence Cluster Universe, Boltzmannstr. 2, D-85748 Garching, Germany; shinya.wanajo@universe-cluster.de
[2] Max-Planck-Institut für Astrophysik, Karl-Schwarzschild-Str. 1, D-85748 Garching, Germany; thj@mpa-garching.mpg.de

Merger scenarios have been disfavored compared to those of CCSNe partly due to discrepancies between Galactic chemical evolution models and the spectroscopic analyses of Galactic halo stars. The low Galactic event rate (7×10^{-6}–3×10^{-4} yr^{-1}, Belczynski et al. 2002) of mergers and the long lifetimes of binary systems ($\sim$ 1 Myr or 100–1000 Myr, Belczynski et al. 2002) are expected to lead to the delayed appearance of r-elements in the Galactic history with too large star-to-star scattering of their abundances (Qian 2000; Argast et al. 2004). These facts seem to be in conflict with the observational results of Galactic halo stars (Honda et al. 2004; François et al. 2007). Banerjee et al. (2011) suggested that the early enrichment of r-elements might be due to neutrino-induced r-processing in the compact helium-shells of CCSNe of low-metallicity stars, and the contribution from mergers could follow only at a higher metallicity. However, recent studies of Galactic chemical evolution based on the hierarchical clustering of sub-halos (Prantzos 2006, also Y. Ishimaru 2011, in preparation) or with various binary population synthesis models (De Donder & Vanbeveren 2004) do not exclude NS-NS and BH-NS mergers as the dominant astrophysical site of the r-process in the early Galaxy. The reason of observed star-to-star scattering only found in r-elements (but not in α and iron-group elements) has not been fully understood, either (Ishimaru & Wanajo 1999; Tsujimoto et al. 1999; Argast et al. 2000; Arnone et al. 2005; Karlsson & Gustafsson 2005; Cescutti 2008). For these reasons, NS-NS and BH-NS mergers cannot be excluded as the primary source of r-elements in the Galaxy. More studies of nucleosynthesis are highly desired.

In this paper, we examine r-process nucleosynthesis in BH-torus winds, which are expected to be common to both NS-NS and BH-NS mergers. There exist few previous studies of nucleosynthesis relevant to these conditions (Surman et al. 2008; Metzger et al. 2009; Caballero 2011), which are based on parametrized outflow conditions. While Metzger et al. (2009) discuss viscously driven mass ejecta, Surman et al. (2008) and Caballero (2011) examined some phenomenologically chosen trajectories leading to at least a weak r-process, but did neither discuss time-dependences nor did provide the integrated abundance distribution or the ejected amount of r-process nuclei. Currently, multi-dimensional simulations of the wind phase after the formation of a stable accretion torus are not yet available. Hence, we adapt a semi-analytic, spherically symmetric, general relativistic steady-state wind model for nucleosynthesis calculations of BH-torus winds. The model has originally been developed for the studies of the r-process in neutrino-driven winds of CCSNe (Wanajo et al. 2001).

Our paper is organized as follows. In § 2, we describe our model of stationary BH-torus winds and discuss basic outcomes derived from the wind solutions. In § 3, a phenomenological, time-evolutionary model of the neutrino luminosities of the torus is introduced, which is needed to determine the initial composition for nucleosynthesis and to calculate the mass-integrated yields as well as the ejecta mass. The results of nucleosynthesis calculations with the wind solutions are then presented in § 4, along with the mass-integrated abundances ejected from the BH torus. In § 5, we discuss the potential role of BH-torus winds as the origin of r-elements in the Galaxy. A summary of the paper follows in § 6.

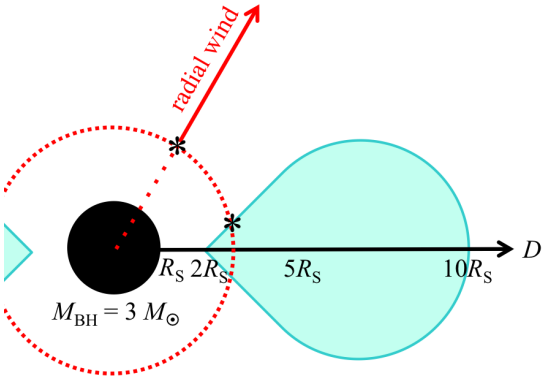

FIG. 1.— Sketch of our model design for BH-torus winds. A rotating BH with the mass $M_{BH} = 3M_\odot$ is located in the center of an accretion torus ("neutrino surface") that lies between $2R_S$ and $10R_S$ from the center, where R_S is the Schwarzschild radius (= 8.86 km). The wind is assumed to be radial. Thus we replace the complex neutrino-surface geometry by a spherical outflow model considering a neutrinosphere with radius $R_\nu = D$ around the gravity center (e.g., the asterisks on the dotted circle).

2. MODELING BH-TORUS WINDS

Our treatment of BH-torus winds is based on the semi-analytic, spherically symmetric, general relativistic model of PNS winds that has been developed for studies of r-process nucleosynthesis by Wanajo et al. (2001). The mass of the central BH is taken to be $M_{BH} = 3M_\odot$, which can be considered as representative of NS-NS mergers (or BH-NS mergers with a low-mass BH, Belczynski et al. 2008). As illustrated in Figure 1, the rotating accretion torus around a spinning BH is defined as the "neutrino surface" and is assumed to lie between $2R_S$ (= 17.7 km) and $10R_S$ (= 88.6 km) from the center (where R_S = 8.86 km is the Schwarzschild radius) as suggested by detailed hydrodynamical simulations of NS-NS and BH-NS merging (e.g., Janka et al. 1999; Ruffert & Janka 1999; Setiawan et al. 2006).

In order to connect the aspherical configuration of the BH-torus system to our spherical model for the wind outflows, an arbitrary point on the torus is replaced by a point on a hypothetical neutrinosphere with the same distance from the center, $R_\nu = D$ (dotted circle in Figure 1). The wind trajectory reaching away from the neutrinosphere, which yields a description of the dynamical and thermodynamical outflow properties, is then derived in the same manner as for spherical PNS winds by solving the general relativistic stationary equations of mass, momentum, and energy conservation (Eqs. (1)-(3) in Wanajo et al. 2001). The Schwarzschild geometry due to the central BH is included here, but the gravitational effects of the torus and wind masses are very small and thus neglected. Rotation of the mass-losing object is neglected as well. The equation of state for ions (ideal gas) and arbitrarily degenerate, arbitrarily relativistic electrons and positrons is taken from Timmes & Swesty (2000). The average neutrino energies are taken to be 15, 20, and 30 MeV, for electron neutrino, electron antineutrino, and heavy-lepton neutrinos, respectively (Janka et al. 1999; Setiawan et al. 2006). The neutrino luminosities of all the flavors are assumed to have the same value L_ν in our wind model. The electron fraction (number of protons

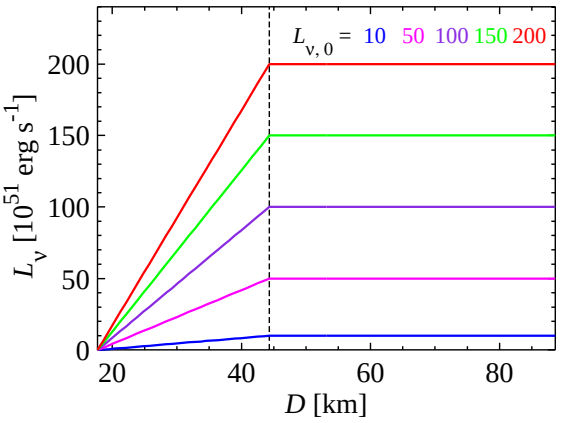

FIG. 2.— Assumed neutrino luminosities (L_ν) as functions of the distance from the center (D). L_ν is assumed to increase linearly from $L_{\nu,0}/100$ to $L_{\nu,0}$ (denoted in the legend in units of 10^{51} erg s^{-1}) between $2R_{\rm S}$ (= 17.7 km) and $5R_{\rm S}$ (= 44.3 km; dotted line) and adopt a constant value at larger distances D.

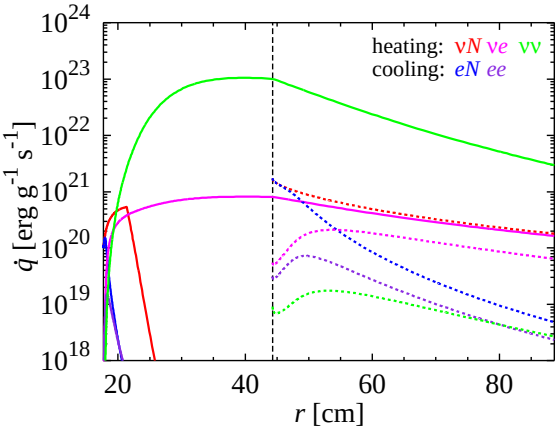

FIG. 3.— Neutrino heating and cooling rates, $\dot{q}$, for the cases with $R_\nu = 2R_{\rm S}$ (solid lines) and $5R_{\rm S}$ (dotted lines) as functions of radius from the center, r. $L_{\nu,0}$ is taken to be 10^{53} erg s^{-1} for both cases. Heating is due to ν_e and $\bar{\nu}_e$ captures on free nucleons (νN), neutrino scattering by e^- and e^+ (νe), and $\nu\bar{\nu}$ pair annihilation to e^-e^+ pairs ($\nu\nu$). Cooling is due to e^- and e^+ captures on free nucleons (eN) and e^-e^+ pair annihilation to $\nu\bar{\nu}$ pairs (ee). The vertical dashed line indicates $D = 5R_{\rm S}$. Note that L_ν increases with r as in Fig. 2 for the $R_\nu = 2R_{\rm S}$ case and that the steep drop of $\dot{q}_{\nu N}$ for this case is due to the decreasing free nucleon abundance by α-particle formation.

per nucleon), $Y_{\rm e}$, is assumed to be 0.5[3]. At the inner boundary, the density is taken to be $\rho = 10^{10}$ g cm^{-3}, and the temperature, T, is taken such that neutrino heating and cooling balance each other ($\sim$ a few MeV). The velocity (or equivalently, mass ejection rate, $\dot{M}$) at the neutrinosphere is determined such that the wind becomes supersonic through a sonic point.

As anticipated from Figure 1, the neutrino flux from the outer regions of the torus is shielded in the vicinity of the BH by the presence of the torus itself. In order to

[3] As described in § 3, $L_{\nu_{\mu,\tau}} \ll L_{\nu_{\rm e}} < L_{\bar{\nu}_{\rm e}}$ and $Y_{\rm e} \ll 0.5$ are expected in the early phase of BH-torus outflows. However, assuming $L_\nu \equiv \frac{1}{2}(L_{\nu_{\rm e}} + L_{\bar{\nu}_{\rm e}})$ for all neutrino kinds and $Y_{\rm e} = 0.5$ is reasonably good for computing the dynamics of BH-torus winds because the wind-driving energy deposition by $\nu_{\rm e}$ and $\bar{\nu}_{\rm e}$ is very similar while that of heavy-lepton ν's is small. Note that these assumptions for L_ν and $Y_{\rm e}$ are applied only in this section.

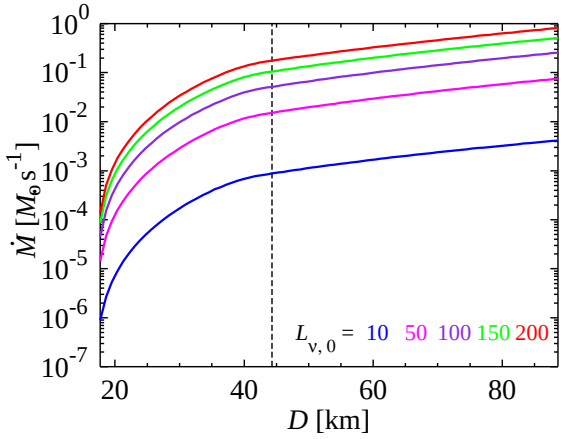

FIG. 4.— Mass ejection rates, $\dot{M}$, from the equivalent neutrinosphere $R_\nu = D$, as a function of D for $L_{\nu,0}$ (in units of 10^{51} erg s^{-1}) denoted in the legend. The vertical dashed line indicates $D = 5R_{\rm S}$.

mimic this effect in our spherical models, we simply assume that L_ν increases linearly from $L_{\nu,0}/100$ to $L_{\nu,0}$ between $2R_{\rm S}$ (= 17.7 km) and $5R_{\rm S}$ (= 44.3 km) and adopts a constant value on the outer side. Figure 2 shows the assumed profiles for selected $L_{\nu,0}$ in units of 10^{51} erg s^{-1}. We define the outflows from $R_\nu < 5R_{\rm S}$ and $R_\nu > 5R_{\rm S}$ as the "inner" and "outer" winds, respectively.

The above assumption of the neutrino luminosity profiles implies fundamental differences in the neutrino heating properties between the inner and outer winds. In Figure 3, the neutrino heating and cooling rates, $\dot{q}$ (in units of erg g^{-1} s^{-1}), for the cases with $R_\nu = 2R_{\rm S}$ (solid lines; representing the innermost winds) and $5R_{\rm S}$ (dotted lines; representing the outer winds) are displayed as functions of the radial distance from the center, r. $L_{\nu,0}$ is taken to be 10^{53} erg s^{-1} for both cases. Heating is due to ν_e and $\bar{\nu}_e$ captures on free nucleons (νN), neutrino scattering by e^- and e^+ (νe), and $\nu\bar{\nu}$ pair annihilation to e^-e^+ pairs ($\nu\nu$). Cooling is caused by e^- and e^+ captures on free nucleons (eN) and e^-e^+ pair annihilation to $\nu\bar{\nu}$ pairs (ee). All the rates are taken from Otsuki et al. (2000, see their Eqs.(8)–(16)), where the gravitational redshift of neutrino energies and the bending of trajectories due to general relativistic effects are fully taken into account.

As can be seen in Figure 3, $\dot{q}_{\nu N}$ dominates the heating rates in the outer winds (dotted lines). The rate $\dot{q}_{\nu e}$ plays only a secondary role, and $\dot{q}_{\nu\nu}$ is negligible. This can also be found in the studies of PNS winds (Qian & Woosley 1996; Otsuki et al. 2000; Thompson et al. 2001). In contrast, in the innermost winds (solid lines), $\dot{q}_{\nu\nu}$ plays the dominant role for heating. This is a consequence of the substantially smaller mass ejection rate, $\dot{M}$ (Fig. 4; defined as that from the corresponding neutrinosphere), driven by the small L_ν from the innermost region of the torus (Fig. 2). This leads to very small values of ρ and also of T in the vicinity of the torus (cf. Wanajo 2006b, for a PNS case). For a given radius r, the heating rates scale with L_ν, ρ, and T according to $\dot{q}_{\nu N} \propto L_\nu$, $\dot{q}_{\nu e} \propto L_\nu \rho^{-1} T^4$, and $\dot{q}_{\nu\nu} \propto {L_\nu}^2 \rho^{-1}$. As a result, the reduction of ρ and T at small r boosts $\dot{q}_{\nu\nu}$ due to radially increasing L_ν (as given in Fig. 2) to much higher values than the other rates (see a similar discussion for anisotropic PNS winds, Wanajo 2006b). Indeed, this has

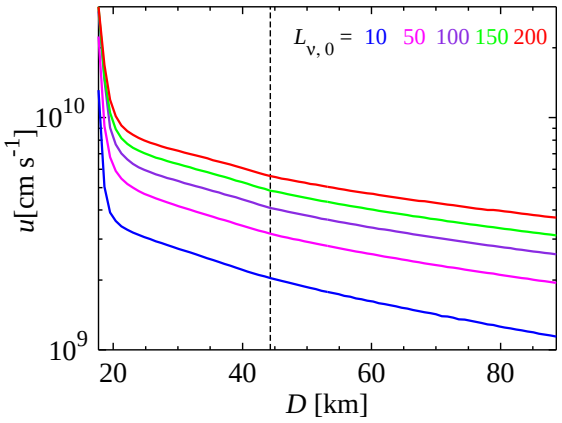

FIG. 5.— Terminal radial velocities as functions of D for $L_{\nu,0}$ (in units of 10^{51} erg s^{-1}) denoted in the legend. The upper bound is the velocity of light. The vertical dashed line indicates $D = 5R_{\rm S}$.

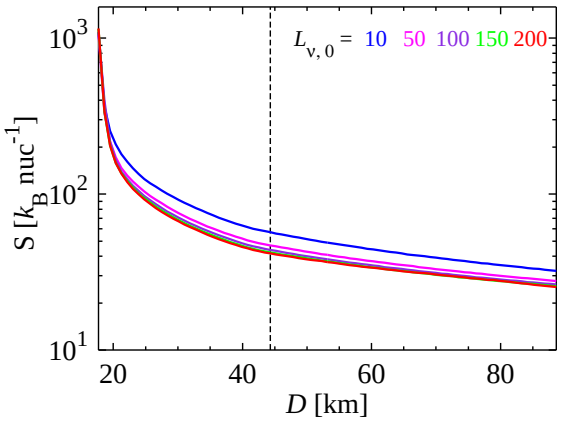

FIG. 6.— Asymptotic entropies as functions of D for $L_{\nu,0}$ (in units of 10^{51} erg s^{-1}) denoted in the legend. The vertical dashed line indicates $D = 5R_{\rm S}$.

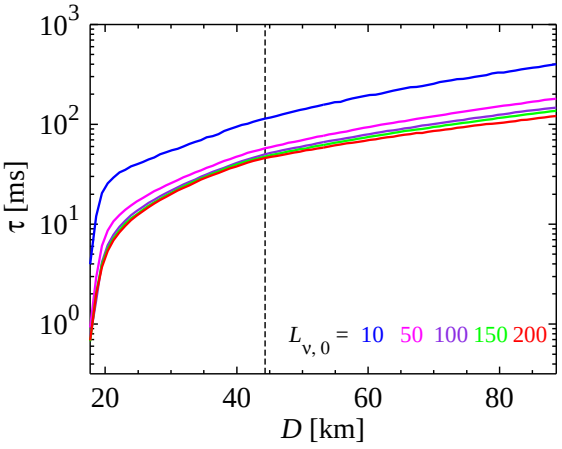

FIG. 7.— Expansion timescales (the e-folding times of temperature below 0.5 MeV) as functions of D for $L_{\nu,0}$ (in units of 10^{51} erg s^{-1}) denoted in the legend. The vertical dashed line indicates $D = 5R_{\rm S}$.

been discussed as a promising mechanism to power short GRB jets presumably arising from NS-NS or BH-NS merging (Ruffert & Janka 1999; Janka et al. 1999, and references therein).

The greater $\dot{q}_{\nu\nu}$ in the inner winds leads to substantially faster (terminal) radial velocities, u, higher asymptotic entropies per nucleon, S, and short expansion timescales, τ (defined as the e-folding time of T below 0.5 MeV). As shown in Figure 5, the innermost winds become relativistic, achieving $u \sim (0.3\text{–}1)\ c$ (where c is the velocity of light). Figures 6 and 7 also show that the innermost winds obtain extremely high S (~ 1000 in units of the Boltzmann constant, $k_{\rm B}$) and short τ (~ 1 ms). In contrast, the outer winds have modest u ($\sim 0.1c$), S ($\sim$ a few 10 $k_{\rm B}$) and τ ($\sim$ a few 100 ms). For a given D, a larger $L_{\nu,0}$ leads to higher u and shorter τ because of the greater neutrino energy deposition. However, the resulting larger $\dot{M}$ reduces the neutrino heating per mass, leading to slightly smaller S.

3. TIME EVOLUTION OF THE BH-TORUS

3.1. *Why is the BH-torus wind neutron-rich?*

As mentioned in § 1, recent hydrodynamical simulations of CCSNe predict that the PNS wind is proton-rich (Fischer et al. 2010; Hüdepohl et al. 2010). The BH-torus wind from "collapsars" (MacFadyen & Woosley 1999) resulting from collapsing rapidly rotating stellar cores is also suggested to be proton-rich (e.g., Kizivat et al. 2010). The BH-torus from NS-NS and BH-NS mergers, originating from decompressed, very neutron-rich NS matter, is different from the collapsar case. The initially neutron-rich torus leads to more production of $\bar{\nu}_{\rm e}$ by e^+ captures on neutrons,

$$n + e^+ \longrightarrow \bar{\nu}_{\rm e} + p, \tag{1}$$

than $\nu_{\rm e}$ production by e^- captures on protons,

$$p + e^- \longrightarrow \nu_{\rm e} + n, \tag{2}$$

and thus one obtains $L_{\bar{\nu}_{\rm e}} > L_{\nu_{\rm e}}$. This allows the BH-torus wind (outside of the torus at lower densities) to remain neutron-rich owing to more $\bar{\nu}_{\rm e}$ captures on free protons,

$$\bar{\nu}_{\rm e} + p \longrightarrow n + e^+, \tag{3}$$

than $\nu_{\rm e}$ captures on free neutrons,

$$\nu_{\rm e} + n \longrightarrow p + e^-. \tag{4}$$

However, despite the fact that the neutrinospheric layers in a PNS are also neutron-rich, the simulations cited above show that PNSs produce essentially equal luminosities of $\nu_{\rm e}$ and $\bar{\nu}_{\rm e}$, resulting in the proton-richness of the ejecta because of the neutron-proton mass difference, which reduces $\bar{\nu}_{\rm e}$ captures compared to $\nu_{\rm e}$ captures. So what exactly is the difference between the PNS and merger BH-torus cases? This can be explained as follows.

For PNSs, the main point is the fact that the PNS is in a phase of *neutronization*. It evolves from more proton-rich (symmetric) initial conditions to more neutron-rich final conditions. In course of this transition, its core radiates more $\nu_{\rm e}$ than $\bar{\nu}_{\rm e}$ (see Eqs. (1) and (2)). On their radial way out of the PNS through highly neutrino-opaque layers this initial $\nu_{\rm e}$ flux is converted into equal $\nu_{\rm e}$ and $\bar{\nu}_{\rm e}$ fluxes by multiple absorption and reemission processes (and μ and τ fluxes of similar size). The escaping $\nu_{\rm e}$ and $\bar{\nu}_{\rm e}$ luminosities are roughly equal because the neutrinospheric layers with their typical densities ($\sim 10^{11}$ g cm^{-3} initially and up to $\sim 10^{13}$ g cm^{-3} at very late times) reach their so-called "β-equilibrium" state (defined by equal number production of $\nu_{\rm e}$ and $\bar{\nu}_{\rm e}$ and

$Y_{\rm e}$ = const. in time) within some tens of milliseconds up to about ~ 100 ms. This is much shorter than the PNS cooling timescale of seconds. On the long PNS evolution timescale the emission is therefore mostly characterized by essentially equal $L_{\nu_{\rm e}}$ and $L_{\bar{\nu}_{\rm e}}$ (with a small difference making sure that there is a net $\nu_{\rm e}$-flux out of the still neutronizing high-density PNS core).

In contrast, the hot post-merger torus is composed of decompressed neutron star matter. It starts out from a very neutron rich initial state and (on its way to a new β-equilibrium condition) *protonizes* gradually (Eq. (1)) because of overall lower densities than it had initially. Since the density and temperature of the torus (on average some 10^{11}–10^{12} g cm^{-3} and about 3–10 MeV) are very similar to the neutrinospheric conditions of a PNS, the protonization of the torus proceeds on the same timescale as the neutronization of the neutrinospheric region in the PNS case. As mentioned above, this typical timescale is tens of milliseconds at the given densities, presumably up to ~ 100 ms. This is exactly a major fraction of the accretion timescale of most of the torus mass into the BH (and is the timescale for the protonization assumed in our simple model described in § 3.2). Because of the protonization, $L_{\bar{\nu}_{\rm e}}$ is higher than $L_{\nu_{\rm e}}$, in inverse analogy to the fact that $L_{\nu_{\rm e}}$ is higher in the case of a collapsing stellar core during the early times when the postshock layer is still on its way to reach the β-equilibrium condition, starting out from a nearly symmetric initial state. For this reason, the neutrino-driven ejecta from the BH-torus are expected to be neutron-rich (see Eqs. (3) and (4)) for a significant duration of the wind phase.

Note that a direct consequence of the fact that the torus conditions in density and temperature are roughly similar to the neutrinospheric conditions in a PNS is the finding that the μ and τ neutrino luminosities are 5–10 times lower than the $\nu_{\rm e}$ and $\bar{\nu}_{\rm e}$ luminosities in the case of the tori (see Janka et al. 1999; Ruffert & Janka 1999). In a PNS the μ and τ neutrinos are produced at much higher densities than $\nu_{\rm e}$ and $\bar{\nu}_{\rm e}$. Such densities are not reached by the accretion tori.

3.2. *Time Evolution of Neutrino Luminosities*

In order to calculate the nucleosynthesis for each wind trajectory, the $Y_{\rm e}$ value of the torus, which defines the initial composition, should be specified. In addition, the ejecta mass for each wind trajectory should be determined to calculate the mass-integrated nucleosynthetic abundances. For this purpose, we assume that the time evolution of $L_{\nu_{\rm e}}$ and $L_{\bar{\nu}_{\rm e}}$ can be written as

$$L_{\nu_{\rm e}}(t) = L_{\nu,{\rm i}} \left(\frac{t}{t_{\rm i}}\right)^{-\beta}, \tag{5}$$

$$L_{\bar{\nu}_{\rm e}}(t) = L_{\nu,{\rm i}} \left(\frac{t}{t_{\rm i}}\right)^{-\beta} \left[1 + 2\left(\frac{t}{t_{\rm i}}\right)^{-\alpha}\right], \tag{6}$$

where $L_{\nu,{\rm i}} = 10^{53}$ erg s^{-1} is chosen as a representative value of the initial neutrino luminosity at $t = t_{\rm i} = 10$ ms (e.g., Janka et al. 1999; Setiawan et al. 2006). The power exponent β is taken to be 1.3 (Metzger et al. 2008; Lee et al. 2009). The value of α is uncertain and for simplicity assumed to be a modest number, $\alpha = 1$, because $L_{\bar{\nu}_e} > L_{\nu_e}$ is expected during a significant time of the torus evolution (§ 3.1). These relations give $L_{\bar{\nu}_{\rm e}}/L_{\nu_{\rm e}} = 3$ at $t = t_{\rm i}$, being in agreement with hydrodynamical results (Janka et al. 1999; Setiawan et al. 2006), and $L_{\bar{\nu}_{\rm e}} = L_{\nu_{\rm e}}$ for $t \gg t_{\rm i}$ (Metzger et al. 2008). Eqs. (5) and (6) yield an approximative time evolution of (the torus-averaged value of) $Y_{\rm e}$ in the protonizing torus (§ 3.1; Eqs. (1) and (2)),

$$\dot{Y}_{\rm e} = \frac{L_{\bar{\nu}_{\rm e}}(t) - L_{\nu_{\rm e}}(t)}{N_{\rm b}\langle\epsilon_\nu\rangle} = \frac{2L_{\nu,{\rm i}}}{N_{\rm b}\langle\epsilon_\nu\rangle}\left(\frac{t}{t_{\rm i}}\right)^{-(\alpha+\beta)}, \tag{7}$$

where $N_{\rm b}$ and $\langle\epsilon_\nu\rangle$ are the total baryon number of the torus and the mean neutrino energy ($\sim$ 18 MeV, Janka et al. 1999; Setiawan et al. 2006) averaged for $\nu_{\rm e}$ and $\bar{\nu}_{\rm e}$. This can be integrated to yield

$$\begin{aligned} Y_{\rm e}(t) &= Y_{\rm e,i} + \frac{2L_{\nu,{\rm i}}}{N_{\rm b}\langle\epsilon_\nu\rangle}\int_{t_{\rm i}}^{t}\left(\frac{t'}{t_{\rm i}}\right)^{-(\alpha+\beta)} dt' \\ &= Y_{\rm e,i} + \frac{2L_{\nu,{\rm i}}\,t_{\rm i}}{(\alpha+\beta-1)N_{\rm b}\langle\epsilon_\nu\rangle}\left[1 - \left(\frac{t}{t_{\rm i}}\right)^{-(\alpha+\beta-1)}\right] \end{aligned} \tag{8}$$

where $Y_{\rm e,i} = 0.05$ is assumed for the initial electron fraction (e.g., Ruffert & Janka 1999). Further assuming that $Y_{\rm e}$ asymptotes to $Y_{\rm e,f} = 0.50$ for $t \gg t_{\rm i}$ (e.g., Metzger et al. 2008), we get

$$\frac{2L_{\nu,{\rm i}}\,t_{\rm i}}{(\alpha+\beta-1)N_{\rm b}\langle\epsilon_\nu\rangle} = Y_{\rm e,f} - Y_{\rm e,i}. \tag{9}$$

This simplifies Eq. (8) to become

$$Y_{\rm e}(t) = Y_{\rm e,f} - (Y_{\rm e,f} - Y_{\rm e,i})\left(\frac{t}{t_{\rm i}}\right)^{-(\alpha+\beta-1)}. \tag{10}$$

Eq. (10) provides $Y_{\rm e}$ of the torus at a given evolutionary time, t. Note that the value of $N_{\rm b}$ (not made use of in this study) can be estimated from Eq. (9) and leads to the approximate torus mass,

$$M_{\rm torus} = N_{\rm b} m_{\rm u} \approx \frac{2L_{\nu,{\rm i}}\,t_{\rm i}\,m_{\rm u}}{(\alpha+\beta-1)(Y_{\rm e,f} - Y_{\rm e,i})\langle\epsilon_\nu\rangle} \sim 0.1 M_\odot, \tag{11}$$

which is consistent with hydrodynamical results of compact binary mergers (e.g., Janka et al. 1999; Ruffert & Janka 1999).

3.3. *Connecting Steady Wind and BH-Torus Evolution Models*

Our description of BH-torus winds in § 2 is based on steady-state solutions for constant $L_{\nu,0}$ and $Y_{\rm e}$. In order to connect the computed wind trajectories to the time-evolving torus model described in § 3.2, we assume

$$L_{\nu,0} = \frac{L_{\nu_{\rm e}}(t) + L_{\bar{\nu}_{\rm e}}(t)}{2}. \tag{12}$$

This is a reasonable assumption because the wind from the outer torus is driven predominantly by $\nu_{\rm e}$ and $\bar{\nu}_{\rm e}$ captures on free nucleons (Fig. 3), whose heating effect is nearly symmetric between $\nu_{\rm e}$ and $\bar{\nu}_{\rm e}$. This is not true for the innermost torus, which however does not significantly contribute to the mass-integrated nucleosynthetic abundances as we will see later. Eq. (12) gives, with Eqs. (5), (6) and (10), $L_{\nu_{\rm e}}$, $L_{\bar{\nu}_{\rm e}}$, t, Δt, and $Y_{\rm e}$ (as the initial value for nucleosynthesis) for a given $L_{\nu,0}$ in

TABLE 1
TIME-EVOLUTION OF THE BH TORUS

j	$L_{\nu,0}$[a]	L_{ν_e}[a]	$L_{\bar{\nu}_e}$[a]	t [ms]	Δt [ms]	Y_e[b]
1	200	100	300	10.0	0.290	0.050
2	190	96.4	284	10.3	0.316	0.066
3	180	92.6	267	10.6	0.346	0.083
4	170	88.9	251	11.0	0.381	0.100
5	160	85.0	235	11.3	0.422	0.118
6	150	81.0	219	11.8	0.471	0.135
7	140	77.0	203	12.2	0.530	0.153
8	130	72.9	187	12.8	0.603	0.172
9	120	68.6	171	13.4	0.692	0.191
10	110	64.3	156	14.1	0.806	0.211
11	100	59.8	140	14.9	0.953	0.231
12	90	55.1	125	15.8	1.15	0.252
13	80	50.3	110	17.0	1.42	0.274
14	70	45.3	94.7	18.4	1.81	0.296
15	60	40.1	79.9	20.2	2.41	0.319
16	50	34.7	65.3	22.6	3.40	0.344
17	40	28.9	51.1	26.0	5.26	0.370
18	30	22.7	37.3	31.3	9.56	0.398
19	20	16.1	23.9	40.8	24.7	0.428
20	10	8.68	11.3	65.6	34.4	0.461

[a] in units of 10^{51} erg s^{-1}.
[b] initial value for nucleosynthesis.

our steady-state model of BH-torus winds. These values are listed in Table 1 for $L_{\nu,0} = 200, 190, \cdots, 10$ (in units of 10^{51} erg s^{-1}). Here, Δt are the time intervals $\Delta t_j = t_{j+1} - t_j$ between the j-th and $(j+1)$-th wind trajectories. For the 20th wind trajectory (last line in Table 1), Δt is determined such that the total evolutionary time becomes $t = 100$ ms.

The mass ejection rate for the j-th value of $L_{\nu,0}$ from the torus region $D_i \le D \le D_{i+1}$ is calculated as

$$\Delta\dot{m}_{i,j} = \frac{\dot{M}_{i,j}}{4\pi D_i^2} 2\pi (D_{i+1}^2 - D_i^2) = \frac{\dot{M}_{i,j}(D_{i+1}^2 - D_i^2)}{2D_i^2}, \quad (13)$$

where the torus is imagined to be a disk, ejecting matter perpendicularly toward the north and south directions. Here, $\dot{M}_{i,j}$ is the mass ejection rate from the corresponding neutrinosphere with $R_\nu = D_i$ (Fig. 4) for the j-th value of $L_{\nu,0}$, and the mass flux density $(\dot{M}_{i,j}/4\pi D_i^2)$ of the spherical wind calculation is weighted by the effective torus surface element in Eq. (13). The mass ejection rate during time interval Δt_j from the entire torus with $L_{\nu,0} = (L_{\nu,0})_j$ is then given as

$$\dot{m}_j = \sum_i \Delta\dot{m}_{i,j}. \quad (14)$$

Eq. (13) with the Δt from Table 1 gives the ejecta mass

$$\Delta m_{i,j} = \Delta\dot{m}_{i,j}\Delta t_j \quad (15)$$

for the wind at $D = D_i$ and with $L_{\nu,0} = (L_{\nu,0})_j$. From Eq. (15) the total ejecta mass in the BH-torus outflow during the first 100 ms is calculated as

$$m_{\rm ej} = \sum_{i,j} \Delta m_{i,j} = 1.96 \times 10^{-3} M_\odot. \quad (16)$$

From Eq. (15) and with the numbers of Table 1, the ejecta mass $\Delta m_{\rm ej}$ (normalized by $m_{\rm ej}$) as a function of u can be constructed in a binned form as histogram (Fig. 8). We find that the sub-relativistic winds with $u \sim 0.1c$ dominate the ejecta. The relativistic ejecta from the innermost torus are essentially unimportant. While the entropies are high, $S \sim$ 100–1000 $k_{\rm B}$, in the innermost winds (Fig. 6), the ejecta with modest entropies, $S \sim 30 k_{\rm B}$, dominate (Fig. 9). Moreover, the winds with modest $\tau \sim 100$ ms dominate, and those with short $\tau \sim$ 1–10 ms make a very small contribution (Fig. 10).

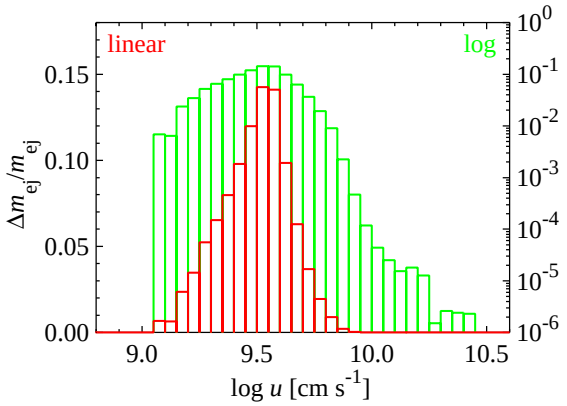

FIG. 8.— Histogram of the ejecta mass distribution $\Delta m_{\rm ej}$ (normalized by the total ejecta mass, $m_{\rm ej}$) in linear (left vertical axis) and logarithmic (right vertical axis) scales as a function of the terminal expansion velocity u (in logarithmic scale).

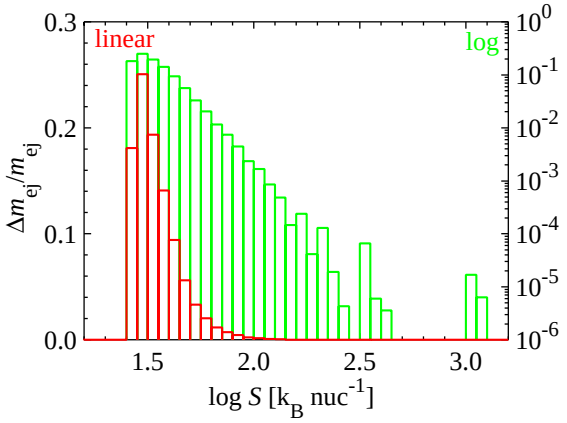

FIG. 9.— Same as Figure 8, but as a function of the asymptotic value of the ejecta entropy S.

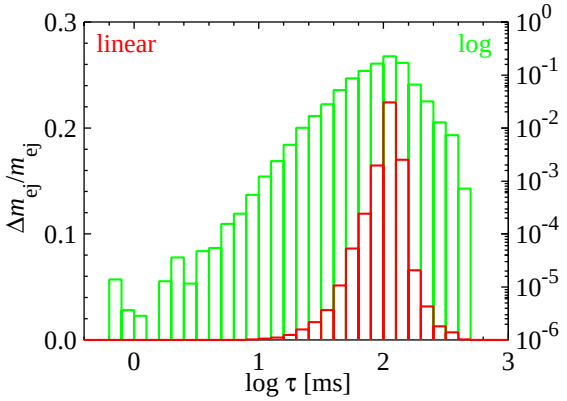

FIG. 10.— Same as Figure 8, but as a function of the expansion timescale τ.

4. NUCLEOSYNTHESIS IN BH-TORUS WINDS

The nucleosynthetic yields in each wind trajectory are computed by solving an extensive nuclear reaction net-

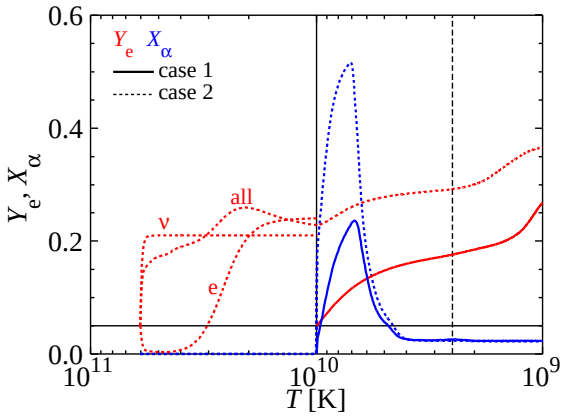

FIG. 11.— Evolution of the electron fraction (Y_e; red) and of the mass fraction of α-particles (X_α; blue) as functions of (decreasing) temperature for case 1 (solid lines; only for $T_9 < 10$) and case 2 (dotted lines). $L_{\nu,0} = 2 \times 10^{53}$ erg s^{-1} and $D = 5R_S$ are taken for both cases. For case 2, three cases of the Y_e evolution are shown (for $T_9 > 10$), in which all four reactions (Eqs. (1)–(4)), only ν_e and $\bar{\nu}_e$ captures on free nucleons (Eqs. (3) and (4)), and only e^- and e^+ captures on free nucleons (Eqs.(1) and (2)) are included (indicated by "all", "ν", and "e", respectively). The horizontal and vertical solid lines indicate, respectively, the initial (torus) Y_e (= 0.05) and $T_9 = 10$ (at which the computation is switched to making use of the full reaction network). The vertical dashed line at $T_9 = 2.5$ indicates where r-processing begins.

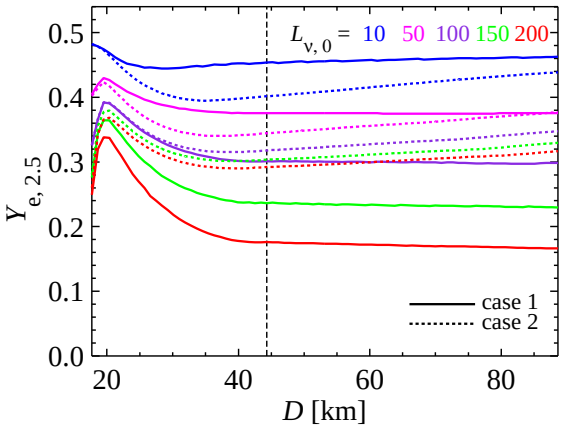

FIG. 12.— Electron fractions for case 1 (solid lines) and case 2 (dotted lines) when the temperature has decreased to 2.5×10^9 K as functions of D for $L_{\nu,0}$ (in units of 10^{51} erg s^{-1}) denoted in the legend. The vertical dashed line indicates $D = 5R_S$.

work code. The network consists of 6300 species between the proton and neutron drip lines, all the way from single neutrons and protons up to the $Z = 110$ isotopes (for more detail, see Wanajo et al. 2011b). Neutrino interactions on free nucleons and α-particles are also taken into account, but fission reactions are not included. As will be described in § 4.3, the effect of (neutron-induced) fission during the r-process is expected to be of minor importance in our explored cases. Our fiducial case ("case 1") is defined by initiating each nucleosynthesis calculation when the temperature decreases to $T_9 = 10$ (where T_9 is the temperature in units of 10^9 K), at which nuclear statistical equilibrium (NSE) is immediately recovered from arbitrary initial compositions. The initial composition we adopt is Y_e and $1 - Y_e$ for free protons and free neutrons, respectively, using the Y_e value of the torus for a given $L_{\nu,0}$ (see Table 1). The calculations are carried out for wind solutions with $L_{\nu,0} = 10$–200 in steps of 10 (in units of 10^{51} erg s^{-1}; Table 1) and $D = (2$–$10)\ R_S = 17.7$–88.6 km with intervals of $0.1R_S = 0.886$ km, i.e., for 1620 trajectories in total.

4.1. *Electron Fractions*

Figure 11 shows the variation of Y_e and of the mass fraction of α-particles, X_α, as functions of (decreasing) temperature for $L_{\nu,0} = 2 \times 10^{53}$ erg s^{-1} and $D = 5R_S$ (case 1; solid lines). This wind trajectory has the lowest initial (torus) Y_e of 0.05 (indicated by a horizontal solid line) of our considered models. As can be seen in Fig. 11, Y_e increases during the early wind expansion phase from its initial value (at $T_9 = 10$; vertical solid line) to $Y_{e,2.5}$ (at $T_9 = 2.5$, considered as corresponding to the onset of the r-process phase; vertical dashed line). This is caused by several effects. The first effect is that, as soon as the nucleosynthesis calculation starts, Y_e relaxes toward the equilibrium value, $Y_{e,a}$ (e.g., Eq. (77) in Qian & Woosley 1996), due to ν_e and $\bar{\nu}_e$ captures on free nucleons (Eqs. (3) and (4)). The asymptotic value for this wind trajectory is $Y_{e,a} = 0.21$. The second effect is associated with the continuous α-particle formation (peaking at $T_9 \approx 7$ in Fig. 11) from recombination of free protons and free neutrons produced by neutrino capture reactions (Eqs. (3) and (4)). This drives Y_e toward 0.5 ("α-effect"; Meyer et al. 1998a). As a result of these combined effects, $Y_{e,2.5}$ (= 0.18) is sizably higher than the initial value of 0.05.

It is important to note that ν_e and $\bar{\nu}_e$ captures on free nucleons (Eqs. (3) and (4)) and also e^- and e^+ captures on free nucleons (Eqs. (1) and (2)) will also operate before the temperature decreases to $T_9 = 10$. We therefore consider another case ("case 2"), in which each nucleosynthesis calculation is started from closer to the neutrinosphere (at $R_\nu = D = 5R_S$ and $T_9 = 60$ in this case) including the four reactions of Eqs. (1)–(4) (labelled "all" in Fig. 11; dotted lines). The computation is then switched to making use of the full reaction network at $T_9 = 10$. Fig. 11 also shows the results when including only ν_e and $\bar{\nu}_e$ captures ("ν"; Eqs. (3) and (4)) and e^- and e^+ captures ("e"; Eqs. (1) and (2)) for $T_9 > 10$. We find that the Y_e immediately jumps to ~ 0.15 mostly by neutrino captures, continues to gradually increase to 0.26 by competition of all four reactions of Eqs. (1)–(4), and decreases slightly toward $Y_{e,a}$ (but still $Y_e = 0.23 > Y_{e,a} = 0.21$ at $T_9 = 10$). The increase of Y_e for $T_9 < 10$ is solely due to the α-effect. As a result, $Y_e = 0.29$ at $T_9 = 2.5$, which is ~ 0.1 higher than that in our fiducial case 1.

Figure 12 shows the Y_e values when the temperature has decreased to $T_9 = 2.5$, $Y_{e,2.5}$, over the entire D range for selected $L_{\nu,0}$ cases (denoted in the legend). The shifts of Y_e from the initial values (see Table 1) are particularly prominent in the inner winds, where the matter experiences a strong α-rich freezeout owing to the high S and short τ (Figs. 6 and 7; cf. Fig. 14). As described above, the $Y_{e,2.5}$ values are significantly different between cases 1 and 2, in particular for the high $L_{\nu,0}$ (i.e., low Y_e) winds.

We emphasize, however, that this is based on our simplified wind models and the exact Y_e evolution for $T_9 > 10$ would be highly dependent on the detailed density structure as well as the highly uncertain neutrino field in the vicinity of the torus, where only transport

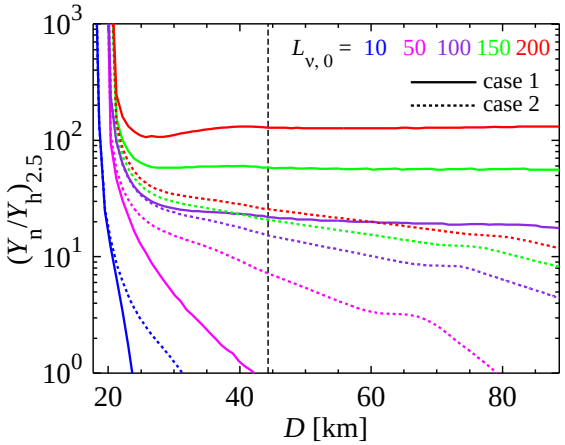

FIG. 13.— Neutron-to-seed ratios (measured at $T_9 = 2.5$) for case 1 (solid lines) and case 2 (dotted lines) as functions of D for $L_{\nu,0}$ (in units of 10^{51} erg s^{-1}) denoted in the legend. The vertical dashed line indicates $D = 5R_S$.

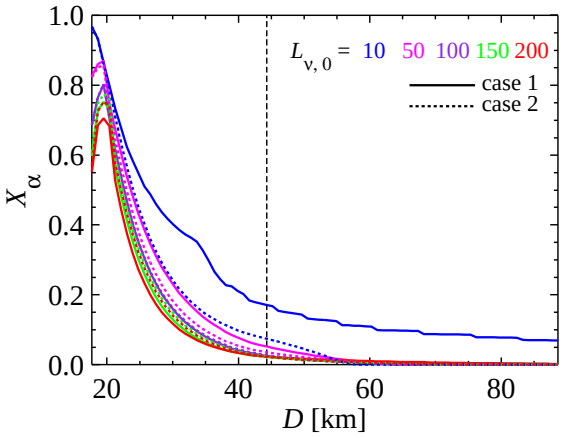

FIG. 14.— Mass fractions of α-particles for case 1 (solid lines) and case 2 (dotted lines) as a function of D for $L_{\nu,0}$ (in units of 10^{51} erg s^{-1}) denoted in the legend. The vertical dashed line indicates $D = 5R_S$.

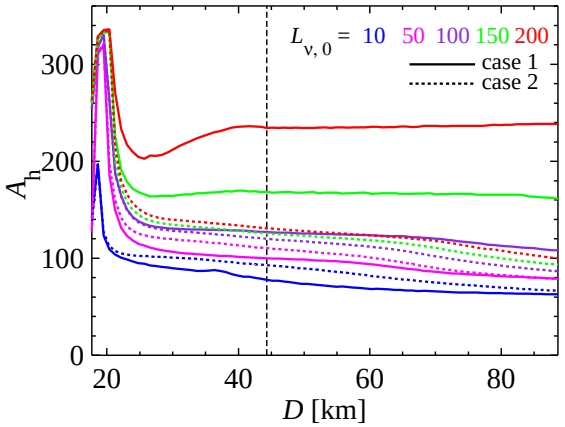

FIG. 15.— Average atomic mass numbers of heavy nuclei ($Z > 2$) for case 1 (solid lines) and case 2 (dotted lines) as functions of D for $L_{\nu,0}$ (in units of 10^{51} erg s^{-1}) denoted in the legend. The vertical dashed line indicates $D = 5R_S$.

calculations can give an appropriate description of the energy and direction distribution of the neutrinos. We therefore consider the $Y_{e,2.5}$ differences between cases 1 and 2 as possible uncertainties of Y_e in this study. As can be seen in Fig. 12, the range of $Y_{e,2.5}$ for case 2 is well bracketed by that for case 1 between $L_{\nu,0} = 10$ and 100 (in units of 10^{51} erg s^{-1}). For this reason, we take case 1 as our fiducial model (and as an optimum case for strong r-processing) in the following sections.

4.2. *Neutron-to-seed Ratios*

The neutron-to-seed ratios at the onset of the r-process (defined at $T_9 = 2.5$), $(Y_n/Y_h)_{2.5}$, are shown in Figure 13. We find sizable $(Y_n/Y_h)_{2.5} > 1000$ (up to $\sim 10^8$; not displayed in Fig. 13) in the innermost region. Except for the inner winds, however, $(Y_n/Y_h)_{2.5}$ is nearly constant with D for $L_{\nu,0} \geq 100$ (in units of 10^{51} erg s^{-1}), being $(Y_n/Y_h)_{2.5} \sim 120$ at most. This is large enough to expect the formation of the third r-process peak ($A = 195$) and beyond, but not fission cycling. A high neutron excess ($Y_{e,2.5} \lesssim 0.2$) is needed for a strong r-process at the modest S ($< 100k_B$; Figure 6) and τ (> 10 ms; Figure 7) for the winds except for the innermost region.

4.3. *α-Particles versus Heavy Nuclei*

Figure 14 shows the mass fractions of α-particles in the final nucleosynthetic abundances (solid lines). In the inner winds, the α concentration is significant owing to the high S and short τ. The r-process thus starts from the seed abundances formed in neutron-rich quasi nuclear equilibrium (QSE; $A \sim 90$, Meyer et al. 1998b). Note that the α-abundances do not change after charged-particle freezeout ($T_9 \sim 4$; Fig. 11). In the innermost winds, the extremely high S and short τ lead to neutron-rich freezeout. This is the reason why $Y_{e,2.5}$ decreases as D approaches the inner tip of the torus (Fig. 12). The low mass fraction of α-particles in the outer winds indicates that the r-process starts from seed abundances formed in conditions close to neutron-rich NSE ($A \sim 80$, Hartmann et al. 1985; Wanajo et al. 2011a). The nucleosynthetic abundances are thus dominated by heavy elements, not by α-particles, in the outer winds.

Figure 15 shows the atomic mass numbers of the final products, A_h, mass-averaged over heavy nuclei with $Z > 2$. We find that A_h is a flat function of D in the outer winds for all $L_{\nu,0}$, similar to $(Y_n/Y_h)_{2.5}$ in Fig. 13. This suggests that in the outer winds the torus-Y_e (assumed to be constant over the entire range of D) predominantly determines A_h, rather than the modest S or τ, which both exhibit gradients with distance D (Figs. 6 and 7). In the innermost winds ($D < 3R_S$), however, the high S and short τ play crucial roles. Except for the innermost winds, A_h ranges from 60 to 220, encompassing nuclei from the trans-iron to the actinide region, but well below the neutron-induced fissioning point ($A \sim 290$, e.g., Fig. 3 in Goriely & Clerbaux 1999). This is a consequence of $Y_{e,2.5} \geq 0.17$ in the outer winds (Fig. 12), which is still too high to expect fission cycling at the modest values of S and τ.

4.4. *Mass-integrated Abundances*

In order to evaluate the net abundances for each $L_{\nu,0}$, the nucleosynthetic yields are mass-integrated over the entire torus range between $D = 2R_S$ and $10R_S$. For the j-th $L_{\nu,0}$, the abundance of nuclide A is calculated with Eqs. (13) and (14) as

$$(Y_A)_j = \frac{1}{\dot{m}_j} \sum_i (Y_A)_{i,j} \Delta \dot{m}_{i,j}. \quad (17)$$

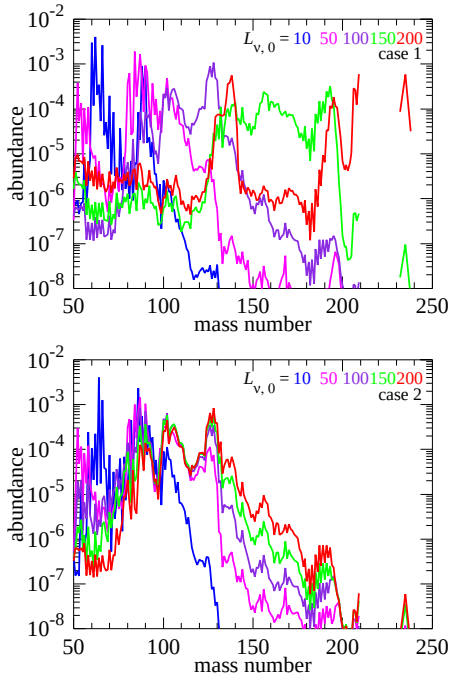

FIG. 16.— Nucleosynthetic abundances for case 1 (top) and case 2 (bottom), mass-integrated between $D = 2R_S$ and $10R_S$, for the values of $L_{\nu,0}$ (in units of 10^{51} erg s^{-1}) denoted in the legend.

Figure 16 shows the mass-integrated nucleosynthetic abundances for selected $L_{\nu,0}$ cases. As noted in § 4.3, the effect of neutron-induced fission is expected to be negligible. In order to roughly include the effect of spontaneous and β-delayed fissions, we simply added the abundances with $A \geq 256$ (all expected to decay by fission) such as

$$Y_{A/2} + 2Y_A \longrightarrow Y_{A/2} \quad (A \geq 256). \tag{18}$$

Actual abundances will depend on the (highly uncertain) decay chains and the abundance distribution of fission fragments. The sharp abundance peak at $A \sim 140$ for $L_{\nu,0} = 2 \times 10^{53}$erg s^{-1} (case 1; solid red line in Fig. 16) is formed by fission fragments. The effect of fission for the other cases are however unimportant.

The time-integrated yield of nuclei of atomic mass number A for the entire torus region is calculated as

$$Y_A = \frac{1}{m_{\rm ej}} \sum_{i,j} (Y_A)_{i,j} \Delta m_{i,j}, \tag{19}$$

making use of Eqs. (15) and (16). In Fig. 17, the resulting yields (solid lines for case 1 and dotted lines for case 2) are compared with the solar system r-process abundances (dots; vertically shifted to match the height of the third r-process peak, $A \approx 195$, for case 1). For case 1, we find good agreement of the calculated abundances with the solar r-process distribution over the entire range of the r-process, $A = 90 - 210$. No overproduction of the $N = 50$ ($A \approx 90$) nuclei can be seen, which were problematic in the wind from PNSs born in SNe (Woosley et al. 1994; Wanajo et al. 2001). This can be understood from the fact that the r-processing in the outer winds of BH-tori starts from NSE (or α-deficient QSE) seeds ($A \sim 80$), rather than from (α-rich) QSE seeds ($A \sim 90$). For case 2, however, the production of heavy r-process elements beyond $A = 130$ drops steeply.

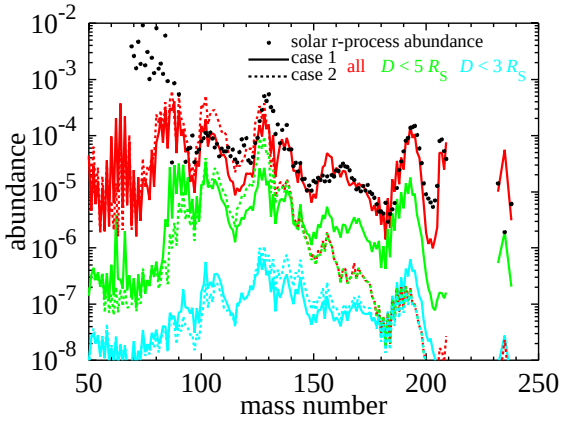

FIG. 17.— Time-integrated nucleosynthetic abundances for the entire torus for case 1 (red solid line) and case 2 (red dotted line). The calculated abundances for case 1 are in good agreement with the solar r-process distribution (dots; scaled to match the 3rd peak height). The contributions from the inner ($D < 5R_S$; green lines) as well as innermost ($D < 3R_S$; light-blue lines) winds are subdominant for case 1, but important for case 2.

Figure 17 also shows the time-integrated abundances from the inner ($D \leq 5R_S$) and innermost ($D \leq 3R_S$) torus. For case 1, we find similar abundance curves for both regions, but with sizably smaller amounts than the total production (10 and 100 times smaller, respectively). This indicates that the low mass ejection rates (Figure 4) from the inner and innermost torus diminish the role of their nucleosynthetic contributions, regardless of their high S and short τ. For case 2, on the other hand, the contributions from inner and innermost regions dominate the abundances heavier than $A \sim 140$.

Note that, for case 1, the deficient Pb ($A = 206$–208) and Bi ($A = 209$) abundances relative to the other r-elements for $D < 5R_S$ (Fig. 17) are due to a fundamental difference in r-processing between the inner and outer winds. The modest τ of an outer wind trajectory leads to an r-process at high temperature ($T_9 \sim 1$), in which case the nucleosynthetic flow approximately follows the path determined by the (n,γ)–(γ,n) equilibrium. In the inner region, however, a shorter τ results in an r-process at substantially lower temperature ($T_9 < 0.5$), in which the flow is determined by the competition between (n,γ) reactions and β-decays ("cold r-process", Wanajo 2007; also Blake & Schramm 1976; Panov & Janka 2009). Wanajo (2007) shows that this non-equilibrium process leads to underabundant Pb.

The ejected mass of r-processed nuclei, defined as those with $A \geq 100$, is derived as

$$m_{r,\rm ej} = m_{\rm ej} \sum_{A \geq 100} A Y_A = \begin{cases} 1.30 \times 10^{-3} M_\odot (\text{case 1}), \\ 1.16 \times 10^{-3} M_\odot (\text{case 2}), \end{cases} \tag{20}$$

showing a dominance of r-processed material (66% and 59% for cases 1 and 2, respectively) in the total ejecta (Eq. (16)). This is a consequence of the fact that the r-process starts from the NSE (or α-deficient QSE) seeds in most cases (§ 4.3). The mass of fission products in the ejecta can be calculated as well,

$$m_{\rm fis,ej} = m_{\rm ej} \sum_{A \geq 256} A Y_A = \begin{cases} 4.25 \times 10^{-5} M_\odot (\text{case 1}), \\ 1.19 \times 10^{-7} M_\odot (\text{case 2}), \end{cases} \tag{21}$$

accounting for only 3% and 0.01% of the total r-process

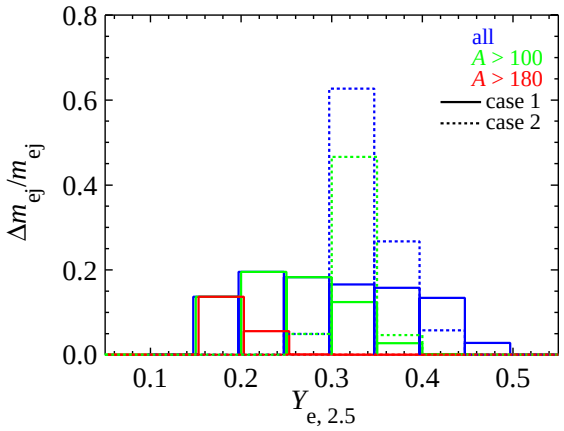

FIG. 18.— Histogram of the ejecta-mass distribution $\Delta m_{\rm ej}$ (normalized by the total ejecta mass, $m_{\rm ej}$) for case 1 (solid lines) and for case 2 (dotted lines) as functions of $Y_{\rm e,2.5}$. Different colors correspond to all ejecta and those with all yields having $A > 100$ and those with all yields having $A > 180$, respectively (slightly shifted in the horizontal direction for visibility).

material for cases 1 and 2, respectively. The mass of Eu in the ejecta, the element taken as representative of r-elements in Galactic chemical evolution studies (e.g., Ishimaru & Wanajo 1999), is estimated to be

$$m_{\rm Eu,ej} = m_{\rm ej} \sum_{A=151,153} A Y_A = \begin{cases} 6.77\times10^{-6} M_\odot ({\rm case\ 1}), \\ 3.98\times10^{-7} M_\odot ({\rm case\ 2}). \end{cases} \quad (22)$$

Figure 18 shows the ejecta-mass histogram as a function of $Y_{\rm e,2.5}$ for case 1 (solid lines) and case 2 (dotted lines). The color coding in Fig. 18 discriminates all abundances, those with all yields having $A > 100$ (all r-abundances), and those with all yields having $A > 180$ (the third peak abundances and heavier). We find that, for case 1, all $Y_{\rm e,2.5}$ values contribute with similar weights to the total abundances. For case 2, the values of $Y_{\rm e,2.5} \approx 0.3$–$0.4$ dominate the total ejecta. Wind trajectories with low $Y_{\rm e}$ are, however, crucial for the production of the r-nuclei with $A > 100$ ($Y_{\rm e,2.5} \lesssim 0.35$), and in particular with $A > 180$ ($Y_{\rm e,2.5} \lesssim 0.20$). This is due to the presence of modest S and τ in the ejecta (Figs. 9 and 10), which demands relatively low $Y_{\rm e}$ values for strong r-processing. Figure 18 also shows that the later wind outflow with $L_\nu < 10^{52}$ erg s^{-1} ($t \gtrsim 100$ ms and $Y_{\rm e} \sim 0.5$), not included in our calculations, would make no relevant contribution to the r-abundances.

5. BH-TORUS WINDS AS THE ORIGIN OF r-ELEMENTS

In § 4, we found that our fiducial model (case 1) of BH-torus winds leads to the full r-process with the solar-like r-pattern for $A = 90$–210. The ejecta mass of the r-processed matter ($A \geq 100$), $m_{r,\rm ej} = 1.30\times10^{-3} M_\odot$ (Eq. (20); case 1), is more than a factor of 10 larger than that needed for CCSNe to be the dominant source of the r-process elements in the Galaxy (Mathews & Cowan 1990). More specifically, the ejected mass of Eu (a nearly pure r-process element), $m_{\rm Eu,ej} = 6.77\times10^{-6} M_\odot$ (Eq. (22); case 1), is a factor of 60 greater than that needed for CCSNe to be the major source of the Galactic Eu (Wanajo & Ishimaru 2006). Provided that our fiducial model (case 1) with $M_{\rm BH} = 3 M_\odot$ and a torus mass of $M_{\rm torus} \sim 0.1 M_\odot$ (Eq. (11)) is representative of NS-NS (or BH-NS) mergers, the canonical CCSN event rate of $\sim 10^{-2}$ yr^{-1} implies that a time-averaged Galactic merger rate of $\sim 2\times10^{-4}$ yr^{-1} would be needed. This is consistent with the upper bound of a merger event rate between 7×10^{-6} and 3×10^{-4} yr^{-1} derived by population synthesis methods for NS-NS and BH-NS binaries (at solar-metallicity conditions, Belczynski et al. 2002) and of statistical results based on binary pulsar surveys (2×10^{-5}–3×10^{-4} yr^{-1}, Kalogera et al. 2004). For case 2 (with inclusion of reactions of Eqs. (1)–(4) at $T_9 > 10$), we find inefficient production of r-elements beyond $A \sim 130$. However, a similar constraint to the Galactic merger rate may be applied for this case, owing to the similar r-processed ejecta mass of $m_{r,\rm ej} = 1.16\times10^{-3} M_\odot$ (Eq. (20); case 2).

It is important to note that the actual ejecta mass of r-abundances could be higher than that we obtained on the basis of our simplified BH-torus wind model. The total ejecta mass, $m_{\rm ej} \approx 2\times10^{-3} M_\odot$ (Eq. (16)), can be even 10 times smaller than that expected from hydrodynamical simulations of compact object mergers (but not of the subsequent BH-torus accretion with its neutrino-driven outflow; Janka et al. 1999). There will be additional contributions from the early mass loss due to the tidal ejection of neutron-rich matter during the merger event (Freiburghaus et al. 1999; Goriely et al. 2005) and neutrino-driven outflows from HMNSs (for the NS-NS case, Dessart et al. 2009) or/and magnetically driven outflows from HMNSs (Rezzolla et al. 2011; Shibata et al. 2011). Moreover, the centrifugal force due to rapid rotation, which we do not take into account, effectively reduces the gravity from the central BH. This could lead to larger mass ejection rates than those obtained here (see Otsuki et al. 2000; Wanajo et al. 2001, for PNS winds). Magnetic fields, which are not considered in our models either, could play a significant role for the mass ejection, producing viscously driven or MHD-driven outflows in addition to the considered neutrino-driven ejecta (Metzger et al. 2009). It should also be noted that the production of heavy r-process elements beyond $A \sim 130$ is marginal if we consider our case 2 to be representative of NS-NS and BH-NS mergers. Case 2 takes into account $\nu_{\rm e}$, $\bar{\nu}_{\rm e}$, e^-, and e^+ captures on free nucleons also for $T_9 > 10$, resulting in significantly higher minimal $Y_{\rm e,2.5}$ (~ 0.3) than that in case 1 (~ 0.2). However, the detailed evolution of $Y_{\rm e}$ will be highly dependent on the density structure and the uncertain neutrino field in the vicinity of the BH-torus, while we consider a simplified spherical wind model and do not have neutrino transport results for BH-tori at bound. Effects of magnetic fields noted above would also modify the evolution of $Y_{\rm e}$. General relativistic effects (which we consider only in the framework of spherically symmetric configurations) can also be important for determining the exact $Y_{\rm e}$ evolution (Caballero 2011). For all these reasons, the nucleosynthetic outcome of this study should be regarded only as suggestive. Future detailed multi-dimensional simulations of NS-NS (or BH-NS) merging, including the later BH-torus wind phase, are required for more quantitative results.

Nevertheless, the good agreement of our nucleosynthesis result for case 1 with the solar r-pattern is encouraging. Such an agreement is also important when one considers compact binary mergers as the origin of early Galactic r-elements in metal-deficient stars with

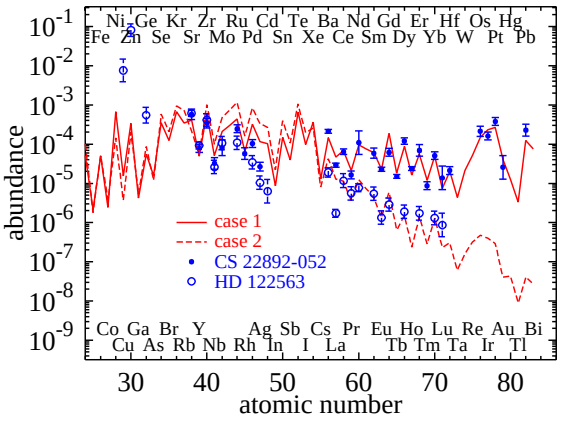

FIG. 19.— Time-integrated nucleosynthetic abundances for the entire torus for case 1 (solid line) and case 2 (dashed line). Cases 1 and 2 are compared with the spectroscopic abundances of r-enhanced (CS 31082-001; filled circles, Sneden et al. 2003) and r-deficient (HD 122563; open circles, Honda et al. 2006) Galactic halo stars, respectively. For HD 122563, the Cd and Lu values are from Roederer et al. (2010) and the Ge value is from Cowan et al. (2005). For both stars, the abundances are vertically shifted to match the calculated Eu abundances.

their uniform (solar-like) r-patterns (Sneden et al. 2008). In Figure 19, the nucleosynthetic abundances for case 1 (solid line; as a function of atomic number) are compared with an r-process enhanced star CS 22892-052 with [Fe/H] ≈ -3.1 (filled circles; scaled to match the calculated Eu abundance, Sneden et al. 2003). We find quite a good agreement of our result with the stellar abundances distribution of CS 22892-052. The good agreement of model and observed abundances is obtained if our BH-torus wind model represents typical NS-NS (or BH-NS) merger events, if the minimal $Y_{\rm e,2.5}$ (at the onset of r-processing) is as low as in case 1 ($\lesssim 0.2$), and if the evolution of $L_{\nu_{\rm e}}$ and $L_{\bar{\nu}_{\rm e}}$ evolutions in Eqs. (5) and (6) is appropriate (e.g., α in Eq. (6) is not very different from unity and $\beta = 1.3$ and the factor of 2 within the bracket of Eq. (6) are good choices). These should be tested by future long-time hydrodynamical simulations of NS-NS and BH-NS merging events and of the evolution of their remnants. Note that, even if the production of r-elements heavier than $A \sim 130$ is marginal as found in case 2, our model could be a possible explanation for the abundance distribution found in an r-process deficient star HD 122563 with [Fe/H] ≈ -2.7 (open circles; scaled to match the calculated Eu abundance, Honda et al. 2006). This suggests that NS-NS and BH-NS mergers could at least be the origin of some trans-iron elements up to $Z \sim 50$ ($A \sim 120$).

For an observational support, future modeling of the Galactic r-element evolution that is not in conflict with spectroscopic results of metal-deficient stars will be important (e.g. Prantzos 2006). In addition, radioactive decays of r-processed ejecta can lead to faint SN-like transients (Li & Paczyński 1998; Metzger et al. 2010; Roberts et al. 2011). Future detections of such signals, possibly as accompanying events of short GRBs, will be a direct support for the occurrence of r-processing in NS-NS and BH-NS mergers. According to the estimates by Metzger et al. (2010), a peak luminosity of $\sim 3 \times 10^{41}$ erg s^{-1} could be expected from the BH-wind ejecta with $m_{r,\rm ej} \sim 1 \times 10^{-3} M_\odot$ (Roberts et al. (2011), however, obtained only slightly higher R-band luminosities for considerably higher ejecta masses). It will be difficult to distinguish the wind component from the early, tidally ejected counterpart. Both could contain similar amounts of radioactive matter. However, the velocities as well as the geometry of the r-processed ejecta might be distinctive between them. Our result implies that the r-processed BH-wind ejecta reach out widely from the torus with velocities of $\sim 0.1c$ (except for the innermost region, Figs. 5 and 8). In contrast, tidal ejecta come from the tips of (one or two) spiral arms, and are expected to achieve larger outgoing velocities ($\gtrsim 0.2c$, Roberts et al. 2011). These could lead to some different features in the light curves (e.g., line profiles or the time of the peak), potentially distinguishable by observations.

6. SUMMARY

We investigated r-process nucleosynthesis in the neutrino-driven outflows from a BH accretion torus (BH-torus winds) formed in NS-NS (or BH-NS) mergers. Different from previous works (Surman et al. 2008; Metzger et al. 2010) we investigated a time- and space-dependent semi-analytic model setup. The BH-torus wind models were constructed by considering spherically symmetric, general relativistic neutrino-driven wind solutions (Wanajo et al. 2001) with the gravitational potential of a central BH of $M_{\rm BH} = 3M_\odot$. The BH accretion torus (around a rotating BH) was assumed to lie between $D = 2R_{\rm S}$ and $10R_{\rm S}$ ($R_{\rm S} = 8.86$ km) from the center. Each wind trajectory reaching away from the torus was obtained by assuming a hypothetical neutrinosphere in the spherical wind model with the radius $R_\nu = D$.

In the innermost wind region ($D \sim 2R_{\rm S}$), the efficient energy deposition due to $\nu\bar{\nu}$ pair annihilation to e^-e^+ pairs leads to very high entropies ($S \gtrsim 100$–$1000 k_{\rm B}$ per nucleon) and short expansion timescales ($\tau \lesssim 1$–10 ms). This allows for a strong r-process regardless of $Y_{\rm e}$ (even with $Y_{\rm e} > 0.5$ when $\tau < 1$ ms, Meyer 2002) or no production of heavy elements (in the relativistic winds with $S \gg 1000 k_{\rm B}$, Lemoine 2002; Beloborodov 2003). However, the small mass ejection from the innermost torus makes this contribution to the total nucleosynthetic abundances essentially negligible. In the outer wind regions ($D > 5R_{\rm S}$), on the other hand, the dominant heating is due to ν_e and $\bar{\nu}_e$ captures on free nucleons as in the case of PNS winds, resulting in modest entropies ($S \sim 30 k_{\rm B}$) and expansion timescales ($\tau \sim 100$ ms). Low $Y_{\rm e}$ values ($\lesssim 0.2$ at $T_9 = 2.5$) are thus essential for a strong r-process. The contribution from outer wind regions dominates the total nucleosynthetic abundances because of their greater mass ejection rates. Note that our BH-torus model does not predict a νp-process (Fröhlich et al. 2006; Pruet et al. 2006; Wanajo 2006a) as suggested in the case of (proton-rich) collapsar disk winds (Kizivat et al. 2010).

The mass-integrated nucleosynthetic abundances, obtained with a phenomenological time evolution of neutrino luminosities, are in good agreement with the solar r-pattern over the entire r-process range of $A = 90-210$, when the neutrino-matter interactions are considered only for $T_9 < 10$ (case 1). This can be taken as the optimal case for strong r-processing in our models. However, when $\nu_{\rm e}$, $\bar{\nu}_{\rm e}$, e^-, and e^+ captures on free nucleons are taken into account also for $T_9 > 10$ (case 2),

the production of heavy r-elements beyond $A \sim 130$ drops off steeply. The total ejecta mass of the BH-torus wind of our simplified model is calculated to be $m_{\rm ej} \approx 2 \times 10^{-3} M_\odot$, in which the r-processed matter dominates ($m_{r,{\rm ej}} \gtrsim 1 \times 10^{-3} M_\odot$). Provided that our BH-torus wind model is representative, NS-NS and BH-NS mergers can produce all (or at least a significant part of) the Galactic r-abundances if the event rate (averaged over the Galactic history) was $\sim 2 \times 10^{-4}$ yr^{-1}, which is consistent with the upper bound of present (solar-metallicity) population synthesis results (7×10^{-6}–3×10^{-4} yr^{-1}, Belczynski et al. 2002) and of statistical results based on binary pulsar surveys (2×10^{-5}–3×10^{-4} yr^{-1}, Kalogera et al. 2004). This implies that BH-torus winds from NS-NS and/or BH-NS mergers could be major (or partial) production sites of the r-process elements in the Galaxy. It should be noted that the actual ejecta mass of r-abundances could be substantially higher than the estimate based on our BH-torus wind model, in which we do not consider any other effects than neutrino-driven outflows, namely, centrifugal force, magnetic fields, or tidally ejected neutron-rich matter from NS disruption.

Obviously, more elaborate hydrodynamical studies of the considered astrophysical site are needed to obtain information of the neutrino field that controls the dynamics as well as the neutron-richness in the BH-torus winds. Note that NS-NS and BH-NS mergers are also suggested to be the sources of short GRBs. An interesting possibility in this context is that the radioactive neutron-rich nuclei ejected during and after mergers might lead to detectable transient electromagnetic signals (Li & Paczyński 1998; Kulkarni 2005; Metzger et al. 2010; Roberts et al. 2011). Studies of Galactic chemical evolution will also be important to test the contributions of NS-NS and BH-NS mergers to the enrichment history of the r-process elements, in particular their role in the early Galaxy.

The project was supported by the Deutsche Forschungsgemeinschaft through the Cluster of Excellence EXC 153 "Origin and Structure of the Universe" (http://www.universe-cluster.de) and the Transregional Collaborative Research Centers on "Neutrinos and Beyond" (SFB/TR27) and on "Gravitational-Wave Astronomy" (SFB/TR7).

REFERENCES

Argast, D., Samland, M., Gerhard, O. E., & Thielemann, F.-K. 2000, A&A, 356, 873
Argast, D., Samland, M., Thielemann, F.-K., & Qian, Y.-Z. 2004, A&A, 416, 997
Arnone, E., Ryan, S. G., Argast, D., Norris, J. E., & Beers, T. C. 2005, A&A, 430, 507
Banerjee, P., Haxton, W. C., & Qian, Y.-Z. 2011, Phys. Rev. Lett., submitted; arXiv1103.1193
Bauswein, A. & Janka, H.-Th. 2011, submitted to Phys. Rev. Lett.; arXiv1106.1616
Belczynski, K., Kalogera, V., & Bulik, T. 2002, ApJ, 572, 407
Belczynski, K., O'Shaughnessy, R., Kalogera, V., Rasio, F., Taam, R. E., & Bulik, T. 2008, ApJ, 680, L129
Beloborodov, A. M. 2003, ApJ, 588, 931
Blake, J. B., & Schramm, D. N. 1976, ApJ, 209, 846
Buras, R., Rampp, M., Janka, H.-Th, & Kifonidis, K. 2006, A&A, 447, 1049
Caballero, O. L, McLaughlin, G. C., & Surman, R. 2011, ApJ, submitted; arXiv:1105.6371
Cowan, J. J., et al. 2005, ApJ, 627, 238
Cescutti, G. 2008, A&A, 481, 691
De Donder, E. & Vanbeveren, D. 2004, New Astron. Rev., 48, 861
Dessart, L., Ott, C. D., Burrows, A., Rosswog, S., & Livne, E. 2009, ApJ, 690, 1681
Farouqi, K., Kratz, K.-L., Pfeiffer, B., Rauscher, T., Thielemann, F.-K., & Truran, J. W. 2010, ApJ, 712, 1359
Fischer, T., Whitehouse, S. C., Mezzacappa, A., Thielemann, F.-K., Liebendörfer, M. 2010, A&A, 517, 80
François, P., et al. 2007, A&A, 476, 935
Frebel, A., Christlieb, N., Norris, J. E., Thom, C., Beers, T. C., & Rhee, J. 2007, ApJ, 660, L117
Freiburghaus, C., Rosswog, S., & Thielemann, F.-K. 1999, ApJ, 525, L121
Fröhlich, C., et al. 2006, ApJ, 637, 415
Goriely, S. & Clerbaux, B. 1999, A&A, 346, 798
Goriely, S., Demetriou, P., Janka, H.-Th., Pearson, J. M., & Samyn, M. 2005, Nucl. Phys. A, 758, 587
Goriely, S., Chamel, N., Janka, H.-T., & Pearson, J. M. 2011, A&A, 531, A78
Hartmann, D., Woosley, S. E., & El Eid, M. F. 1985, ApJ, 297, 837
Hillebrandt, W., Nomoto, K., & Wolff, G. 1984, A&A, 133, 175
Hoffman, R. D., Woosley, S. W., & Qian, Y.-Z. 1997, ApJ, 482, 951
Hoffman, R. D., Müller, B., & Janka, H.-T. 2008, ApJ, 676, L127
Honda, S., et al. 2004, ApJ, 607, 474
Honda, S., Aoki, W., Ishimaru, Y., Wanajo, S., & Ryan, S. G. 2006, ApJ, 643, 1180
Hüdepohl, L., Müller, B., Janka, H.-Th., Marek, A., Raffelt, G. G 2009, Phys. Rev. Lett., 104, 251101
Ishimaru, Y. & Wanajo, S. 1999, ApJ, 511, L33
Janka, H.-T., Eberl, T., Ruffert, M., & Fryer, C. L. 1999, ApJ, 527, L39
Janka, H.-Th., Müller, B., Kitaura, F. -S., & Buras, R. 2008, A&A, 485, 199
Kalogera, V., et al. 2004, ApJ, 601, L179
Karlsson, T. & Gustafsson, B. 2005, A&A, 436, 879
Kitaura, F. S., Janka, H.-Th., & Hillebrandt, W. 2006, A&A, 450, 345
Kizivat, L.-T., Martínez-Pinedo, G., Langanke, K., Surman, R., & McLaughlin, G. C. 2010, Phys. Rev. C, 81, 025802
Kulkarni, S. R. 2005, arXiv:astro-ph/0510256
Lattimer, J. M. & Schramm, D. N. 1974, ApJ, 192, L145
Lattimer, J. M. & Schramm, D. N. 1976, ApJ, 210, 549
Lattimer, J. M., Mackie, F., Ravenhall, D. G., & Schramm, D. N. 1977, ApJ, 213, 225
Lee, W. H., Ramirez-Ruiz, E., & López-Cámara, D. 2009, ApJ, 699, L93
Lemoine, M. 2002, A&A, 390, L31
Li, L.-X. & Paczyński, B. 1998, ApJ, 507, L59
MacFadyen, A. I. & Woosley, S. E. 1999, ApJ, 524, 262
Marek, A. & Janka, H.-Th. 2009, ApJ, 694, 664
Mathews, G. J. & Cowan, J. J. 1990, Nature, 345, 491
Meyer, B. S., McLaughlin, G. C., & Fuller G. M. 1998a, Phys. Rev. C, 58, 3696
Meyer, B. S., Krishnan, T. D., & Clayton, D. D. 1998b, ApJ, 498, 808
Meyer, B. S. 2002, Phys. Rev. Lett., 89, 231101
Metzger, B. D., Piro, A. L., & Quataert, E. 2008, MNRAS, 390, 781
Metzger, B. D., Piro, A. L., & Quataert, E. 2009, MNRAS396, 304
Metzger, B. D., et al. 2010, MNRAS, 406, 2650
Meyer, B. S. 1989, ApJ, 343, 254
Ning, H., Qian, Y.-Z., & Meyer, B. S. 2007, ApJ, 667, L159
Oechslin, R., Janka, H.-T., & Marek, A. 2007, A&A, 467, 395O
Otsuki, K., Tagoshi, H., Kajino, T., & Wanajo, S. 2000, ApJ, 533, 424
Panov, I. V. & Janka, H.-Th. 2009, A&A, 494, 829
Plez, B., et al. 2004, A&A, 428, L9

Prantzos, N. 2006, in Proceedings of the International Symposium on Nuclear Astrophysics - Nuclei in the Cosmos - IX. 25-30 June 2006, CERN., p.254.1
Pruet, J., Hoffman, R. D., Woosley, S. E., Buras, R., & Janka, H.-Th. 2006, ApJ, 644, 1028
Qian, Y.-Z. & Woosley, S. E. 1996, ApJ, 471, 331
Qian, Y.-Z. 2000, ApJ, 534, L67
Rezzolla, L., Giacomazzo, B., Baiotti, L., Granot, J., Kouveliotou, C., & Aloy, M. A. 2011, ApJ, 732, L6
Roberts, L. F., Kasen, D., Lee, W. H., & Ramirez-Ruiz, E. 2011, ApJ, submitted; arXiv1104.5504
Roederer, I. U., Kratz, K.-L., Frebel, A., Christlieb, N., Pfeiffer, B., Cowan, J. J., & Sneden, C. 2009, ApJ, 698, 1963
Roederer, I. U., Sneden, C., Lawler, J. E., & Cowan, J. J. 2010, ApJ, 714, L123
Rosswog, S., Liebendörfer, M., Thielemann, F.-K., Davies, M. B., Benz, W., & Piran, T. 1999, A&A, 341, 499
Ruffert, M. & Janka, H.-T. 1999, A&A, 344, 573
Ruffert, M. & Janka, H.-T. 2010, A&A, 514, 66
Sekiguchi, Y., Kiuchi, K., Kyutoku, K., & Shibata, M. 2011, arXiv1105.2125
Setiawan, S., Ruffert, M., & Janka, H.-Th. 2006, A&A, 458, 553
Shibata, M. & Uryū, K. 2000, Phys. Rev. D, 61, 064001
Shibata, M. & Taniguchi, K. 2006, Phys. Rev. D, 73, 064027
Shibata, M. & Uryū, K. 2006, Phys. Rev. D, 74, 121503
Shibata, M., Suwa, Y., Kiuchi, K., & Ioka, K. 2011, ApJ, 734, L36
Sneden, C., et al. 2003, ApJ, 591, 936
Sneden, C., Cowan, J. J., & Gallino, R. 2008, ARA&A, 46, 241
Sumiyoshi, K., Terasawa, M., Mathews, G. J., Kajino, T., Yamada, S., & Suzuki, H. 2001, ApJ, 562, 880
Surman, R., McLaughlin, G. C., Ruffert, M., Janka, H.-Th., & Hix, W. R. 2008, ApJ, 679, L117
Takahashi, K., Witti, J., & Janka, H.-T. 1994, A&A, 286, 857
Timmes, F. X. & Swesty, F. D. 2000, ApJS, 126, 501
Thielemann, F.-K., et al. 2011, Prog. Part. Nucl.Phys., 66, 346
Thompson, T. A., Burrows, A., & Meyer, B. S. 2001, ApJ, 562, 887
Tsujimoto, T., Shigeyama, T., & Yoshii, Y. 1999, ApJ, 519, L63
Wanajo, S., Kajino, T., Mathews, G. J., & Otsuki, K. 2001, ApJ, 554, 578
Wanajo, S., Tamamura, M., Itoh, N., Nomoto, K., Ishimaru, I., Beers, T. C., & Nozawa, S. 2003, ApJ, 593, 968
Wanajo, S. 2006, ApJ, 647, 1323
Wanajo, S. 2006, ApJ, 650, L79
Wanajo, S. & Ishimaru, I. 2006, Nucl. Phys. A, 777, 676
Wanajo, S. 2007, ApJ, 666, L77
Wanajo, S., Nomoto, K., Janka, H.-T., Kitaura, F. S., Müller, B. 2009, ApJ, 695, 208
Wanajo, S., Janka, H.-T., & Müller, B. 2011, ApJ, 726, L15
Wanajo, S., Janka, H.-T., & Kubono, S. 2011, ApJ, 726, L15
Woosley, S. E., Wilson, J. R., Mathews, G. J., Hoffman, R. D., & Meyer, B. S. 1994, ApJ, 433, 229